A Terrain Slope Estimation Scheme using Infrared Camera for Planetary Exploration Rovers

Satoshi Watanabe
Chuo University
1-13-27 Kasuga, Bunkyo-ku,
Tokyo 112-8551 Japan
+81-3-3817-1845
s_watanabe@ac.jaxa.jp

Kyohei Otsu
Jet Propulsion Laboratory
4800 Oak Grove Dr.
Pasadena, CA 91109
818-354-4321
kyohei.otsu@jpl.nasa.gov

Masatsugu Otsuki
ISAS/JAXA
3-1-1 Yoshinodai, Chuo-ku,
Sagamihara, Kanagawa
252-5210 Japan
+81-50-3362-3024
otsuki.masatsugu@jaxa.jp

Takashi Kubota
ISAS/JAXA
3-1-1 Yoshinodai, Chuo-ku,
Sagamihara, Kanagawa
252-5210 Japan
+81-50-3362-3657
kubota.takashi@jaxa.jp

Gakuto Masuyama
Meijo University
1-501 Shiogamaguchi, Tenpaku-ku,
Nagoya, Aichi 468-8502 Japan
+81-52-832-1235
masuyama@meijo-u.ac.jp

Kazunori Umeda
Chuo University
1-13-27 Kasuga, Bunkyo-ku,
Tokyo 112-8551 Japan
+81-3-3817-1826
umeda@mech.chuo-u.ac.jp

Abstract—**Planetary exploration rovers face severe energy and safety restrictions, which have a strong connection with terrain slopes. During a steep slope traverse, a rover consumes more power and is exposed to higher risks of getting stuck or of overturning. It is essential for a rover to autonomously recognize and avoid steep slopes for efficient and safe operations. Existing techniques (*e.g.* stereo vision) do not completely address challenges in planetary exploration, such as low-textured terrain appearance and computational resource limitations. This paper presents a novel slope estimation method using a monocular infrared camera. The proposed method estimates slope normals based on surface temperatures on two different slopes. The surface energy model is employed to correlate thermal properties to geometrical properties of the terrain. The idea behind this approach is that the solar radiation, which is a major energy source for terrains, can differ by time, slope angles and directions. The difference in energy input generates the gap of surface temperatures between target and reference surfaces, which can be remotely detected with an infrared camera. The proposed method avoids the problem of terrain appearance as it only uses temperature measurements, and is also computationally efficient thanks to efficient preprocessing. The algorithm is validated through simulations and outdoor experiments. The results show the effectiveness of the proposed scheme to estimate terrain slope normals solely from temperature measurements.**

Table of Contents

1. Introduction

The detailed exploration of planetary surfaces has been conducted in the last decades using mobile platforms called *rovers*. The strength of rovers lies in the possibility to travel over many kilometers while carrying scientific instruments to detect and investigate geological interests in another planet. However, the mobility on planetary surfaces brings challenges with it, especially on slopes. A wheeled vehicle can easily lose its mobility on a steep slope due to the loss of traction or kinematic stability. For example, the Mars Exploration Rover (MER) Spirit has ended its mission by losing wheel's traction with soft soil on a slope. Another challenge arises from limited energy availability. If a rover consumes excessive energy along a slope traversal and reduces its travel distance per time, it will decrease the possibility to accomplish all assigned tasks in a limited mission timeline. Therefore, it is essential for a rover to autonomously recognize and avoid steep slopes for safe and efficient exploration.

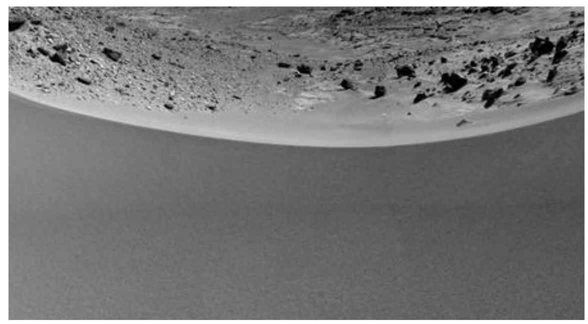

Figure 1. An example of low-textured terrain on Mars (Image by NASA/JPL)

The slope detection problem is an instance of geometrical reconstruction problems, which have been extensively studied in the field of computer vision. In the context of planetary exploration, the slope analysis is typically performed with stereo matching of visible images [1], [2], [3]. Various methods have been proposed in the literature, some of which are compared in [4]. The estimation accuracy of visual stereo matching degrades in low-textured terrain due to the lack of salient features (see Figure 1 for an example of low-textured terrain appearance). There are other approaches such as laser range finders [5] and shape from shading [6], [7]; however, these methods have limitations including the high power consumption and the heavy computational cost.

978-1-5386-2014-4/18/$31.00 ©2018 IEEE

(a) Visual image

(b) Thermal image

Figure 2. Visual and thermal images at the same U-shaped slope

In terms of the computational cost, Spirit rover and Mars Science Laboratory (MSL) Curiosity rover have a 22-MIPS, 20 [MHz], RAD6000 CPU and a 400-MIPS, 200 [MHz], RAD750 CPU, respectively. The performance of these CPU is much lower than that of the modern one, therefore it is important for the rovers to reduce the computational cost.

This paper proposes a new terrain slope estimation method using a monocular infrared camera. The proposed method is based on the observation that the energy input in each terrain region varies depending on the solar incidence angle, and that this energy gap appears as a difference in thermal properties. Figure 2 shows a thermal image of a U-shaped slope captured by an infrared camera. The terrain regions perpendicular to the solar ray direction (image left) has higher temperature measurements than the other regions (right).

In order to formulate the relationship between the thermal and geometrical properties of a terrain, an approach using a surface energy model and a celestial motion model is proposed. Specifically, the proposed method estimates the normal vector of inclined surface by comparing model- and measurement-based energy amounts. The proposed method can avoid the problem of terrain appearance since it relies only on the surface temperature. The proposed scheme is also computationally efficient by leveraging preprocessing.

The rest of this paper is organized as follows. Section 2 explains the energy balance model of the surface. Section 3 discusses the terrain slope estimation procedure. The results of terrain slope estimation through simulation and outdoor experiments are discussed in Section 4 and Section 5, respectively. Finally, the conclusion and future works are described in Section 6.

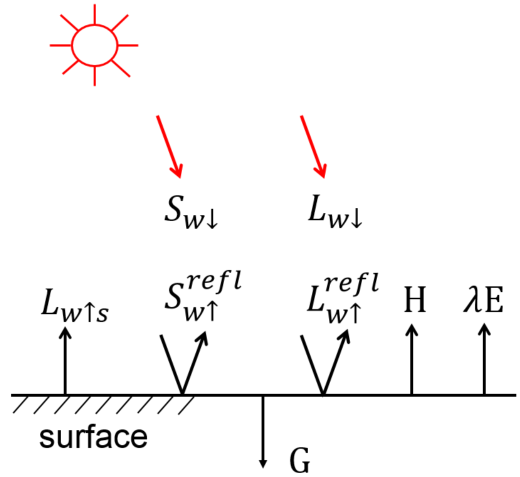

Figure 3. Energy balance model of a ground surface

2. Energy Model

This paper uses the POST thermal model described in [8]. In this model, the energy balance equation of a surface can be written as

$$S_{w\downarrow} + L_{w\downarrow} - L_{w\uparrow s} - S_{w\uparrow}^{refl} - L_{w\uparrow}^{refl} - H - \lambda E - G = 0 \quad (1)$$

The definition of the symbols are given as follows.

Energy inputs:

- Direct solar radiation $S_{w\downarrow}$
- Atmospheric radiation $L_{w\downarrow}$

Energy outputs:

- Emitted long-wave radiation from the surface $L_{w\uparrow s}$
- Reflected solar radiation from the surface $S_{w\uparrow}^{refl}$
- Reflected atmospheric radiation $L_{w\uparrow}^{refl}$
- Sensible heat flux H
- Flux of moisture λE
- Ground flux G

The graphical representation of the energy balance is shown in Figure 3.

As shown in Figure 4, the solar radiation depends on the surface normal and solar direction. The solar radiation is given by

$$S_{w\downarrow} = S\cos\theta \quad (2)$$

where S and θ denote the Direct Normal Irradiance (DNI) and the solar incidence angle, respectively. The DNI is the amount of solar radiation that depends on the time and the location but is independent from the surface geometry. The surface reflectance of the solar radiation is then expressed using a surface albedo A.

$$S_{w\uparrow}^{refl} = AS_{w\downarrow} \quad (3)$$

Some of energy emission terms depend on the terrain temperature T: the long-wave radiation

$$L_{w\uparrow s} = \epsilon\sigma T^4 \quad (4)$$

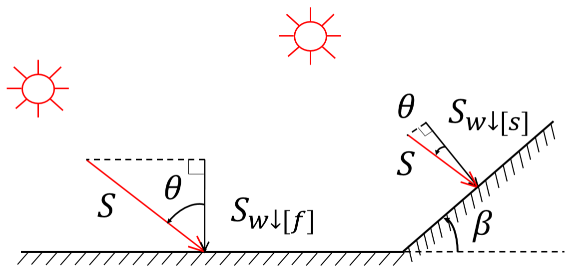

Figure 4. Direct solar radiation in flat surface and slope

where ϵ and σ denote the emissivity of a surface and the Stefan-Boltzmann constant, respectively; and the heat flux

$$H = C_p \rho C_H U (T - T_a) \tag{5}$$

where C_p, ρ, $C_H U$, and T_a denote the specific heat capacity of air at constant pressure, the density of air, an exchange coefficient of heat flux, and an air temperature, respectively.

In order to estimate the geometry from the energy balance equation in (1), the following assumptions are made:

- The surface characteristics are locally uniform.
- The terrain parameters are preliminary identified.
- The following terms are independent of surface geometry: the atmospheric radiation $L_{w\downarrow}$, the reflection atmospheric radiation $L_{w\uparrow}^{refl}$, the flux of moisture λE, and the ground flux G.

Under these assumptions, the relative solar radiation to a reference slope can be obtained from the above definitions. The subtraction of (1) for target and reference terrain gives

$$S_{w\downarrow} - \hat{S}_{w\downarrow} = \alpha(T^4 - \hat{T}^4) + \beta(T - \hat{T}) \tag{6}$$

with terrain-dependent constants $\alpha = \epsilon\sigma/(1 - A)$ and $\beta = C_p \rho C_H U/(1 - A)$. Note that the subtraction eliminates all unknowns from the energy balance equation. As a result, the solar radiation difference can be estimated from the target and reference temperatures T and $\hat{T}$. For simplicity, a flat horizontal plane is used as the reference terrain in the rest of this paper.

3. Slope Estimation Procedure

Slope angles are determined by the following 4 steps.

Step 1. Measure surface temperatures at a reference flat terrain and at a target slope.
Step 2. Estimate the difference of solar radiation between the two terrains using surface temperatures and the energy balance equation.
Step 3. Extract the candidates for slope normals by comparing the estimated radiation difference to the celestial simulation.
Step 4. Continue from step 1 at varying time until the most likely candidate is found.

Estimate the difference of solar radiation from temperatures (Step 1 and 2)

Target and reference surface temperatures are remotely measured using an infrared camera. A reference point (flat terrain) is chosen from past remote or proximity measurements.

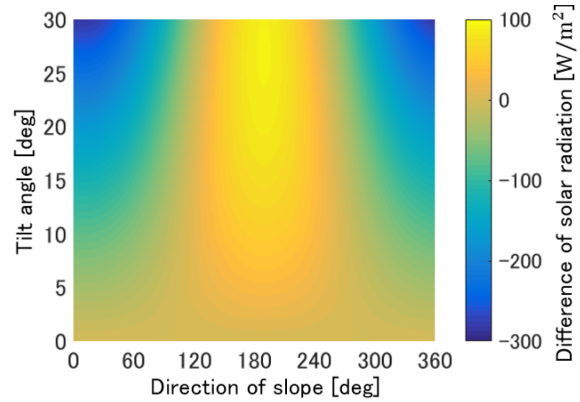

Figure 5. Solar radiation difference against reference terrain at noon at a location in the northern hemisphere.

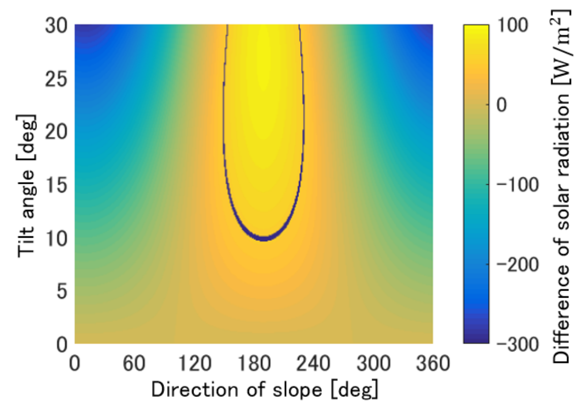

Figure 6. Solar radiation contour overlaid on radiation table. Points along the contour represent the possible candidates of slope angles.

By applying the differential energy balance equation in (6) to the measured temperatures, the relative solar radiation is obtained as a numeric value.

Extract all possible surface normals (Step 3)

All candidates for slope normals are extracted by comparing the estimated radiation difference to the celestial simulation at the same time and location. For the sake of computational efficiency, the difference of solar radiation is precomputed and stored in data tables. The table generation process is summarized as follows.

1) Compute the sunlight vectors at the location for different time based on a celestial simulation.
2) Determine the solar incidence angles for all considered surface normals by computing the vector inner product.
3) Compute the direct solar radiation using (2).
4) Store the subtraction of target and reference solar radiation in data tables.

An example of visualized solar radiation table is shown in Figure 5. The direction of the slope is defined as the azimuth of surface normal. In this paper, the northward direction is defined as 0 [deg] (360 [deg]), and the angle increase clockwise. All the points along the contour line of the estimated radiation difference are marked as candidates, as shown in Figure 6.

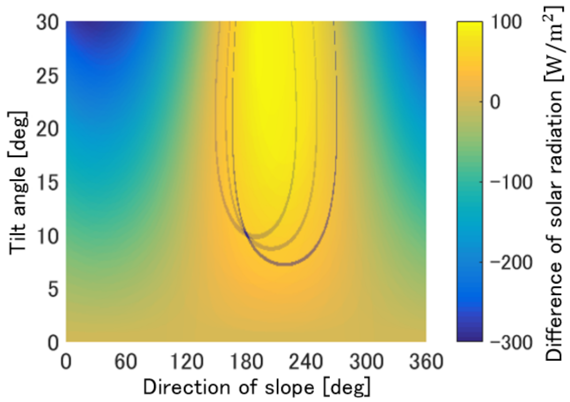

Figure 7. Solar radiation contours at 0:00 pm, 0:30 pm, and 1:00 pm. The intersection represents the true value (direction=180 [deg] and tilt=10 [deg]).

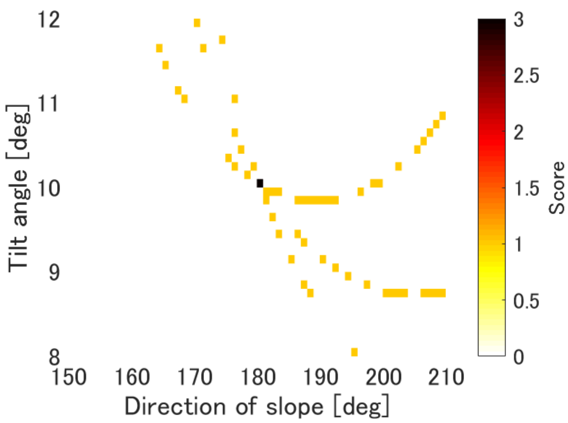

Figure 8. The result of scoring in Figure 7. The point with the maximum score is the intersection.

Select most-likely candidate from multiple measurement (Step 4)

Finally, the most-likely slope normal is selected based on scoring from multiple measurement. The underlying fact is that the sun position changes every minute, while a slope tilt angle and direction at the point is static. The slope normal is estimated by determining the intersection of radiation contours at varying times. Figure 7 exemplifies the intersection of radiation contours. Three curves correspond to the radiation contours at 0:00 pm, 0:30 pm, and 1:00 pm. The intersection is found by scoring. All candidates get score 1 at each measurement. This process is repeated several times at varying times, then the intersection earns the highest score over a given threshold as shown in Figure 8.

4. Simulation Study

A simulation study is conducted to validate our method. The date and the location are set to August 30, 2017 and a point in Earth's northern hemisphere (latitude: 35.558675 [deg], longitude: 139.395232 [deg], altitude: 9.0 [m]), which is the same conditions as the following outdoor experiment. In the simulation, surface temperatures are synthesized based on the simplified energy balance equation

$$(1 - A)S_{w\downarrow} + \epsilon L_{w\downarrow} - \epsilon\sigma T^4 - C_p \rho C_H U(T - T_a) = 0 \quad (7)$$

Table 1. Simulation parameters. JMA represents the dataset from Japan Meteorological Agency.

Name	**Symbol**	**Value**
Surface albedo	A	0.20
Surface emissivity	ϵ	0.90
Heat capacity	C_p	1.00 [kJ/(kg · K)]
Air density	ρ	1.21 [kg/m^3]
Heat exchange coefficient	$C_H U$	0.015 [m/s]
Air temperature	T_a	JMA
Atmospheric radiation	$L_{w\downarrow}$	JMA
Direct normal irradiance	S	JMA

that incorporates the following approximations

- Moisture on surface does not evaporate (i.e., $\lambda E = 0$).
- Heat is not transmitted to the underground (i.e., $G = 0$).

A dataset from Japan Meteorological Agency (JMA) [9] is used for the DNI S, atmospheric radiation $L_{w\downarrow}$ and air temperature T_a. The parameters used in the simulation are summarized in Table 1.

Data points are generated for tilt angles from 0 to 30 [deg] in 0.5 [deg] steps and directions from 0 to 360 [deg] in 1.0 [deg] steps. In other words, there are 61 × 361 patterns of surface geometry. The slope angle estimation is evaluated by the Mean Absolute Error (MAE)

$$\mathrm{MAE} = \frac{1}{n}\sum_{i=1}^{n}|y_i - x_i| \quad (8)$$

and the Standard Deviation (SD) of the absolute error

$$\mathrm{SD} = \frac{1}{n}\sqrt{\sum_{i=1}^{n}(|y_i - x_i| - \mathrm{MAE})^2} \quad (9)$$

where x and y denote actual and estimated slope angles and n denotes the number of estimated slope angles.

Slope estimation results

The proposed method was analyzed statistically for all slope patterns in different time of a day. For each slope pattern, temperatures were measured for 20 minutes at 1-minute intervals. Figure 9 represents the cumulative probability of angle estimation error at each time. The cumulative probability represents the ratio of patterns that can be estimated within an absolute error. For example, 90% of observations has error below 0.43, 0.62, 0.9 [deg] on 9:00 am, 0:00 pm, 3:00 pm, respectively. It can be seen that the proposed estimation method can reliably identify slope angles with a certain accuracy based on temperature measurements.

Direction dependency analysis

The solar incidence angle is important to the proposed algorithm since it directly affects the amount of direct solar radiation. The expected estimation accuracy will change depending on the direction of slope, even at the same moment. Direction dependency was analyzed in Figure 10, which shows the MAE of slope angles for every 30 [deg] at different sunlight conditions. Overall, the absolute error at the south is larger than the one at other directions. One of

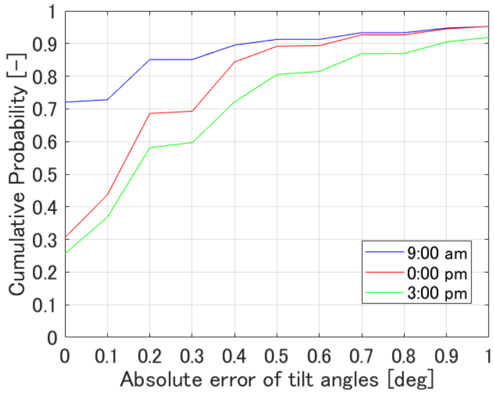

Figure 9. Cumulative probability of absolute error in slope estimation

Table 2. Solar incidence angles in degrees on August 30 and December 11

Local Date (2017)	Tilt angle [deg]	Local Time (pm)			
		0:00	1:00	2:00	3:00
August 30	0 (Flat)	26.9	31.9	41.0	52.1
	10 (Slope)	17.1	24.7	36.5	49.5
	20 (Slope)	7.8	19.9	34.1	48.5
December 11	0 (Flat)	58.8	61.9	67.8	75.9
	5 (Slope)	53.9	57.3	63.8	72.6
	15 (Slope)	44.0	48.2	56.0	66.2
	25 (Slope)	34.1	39.4	48.7	60.2

the reasons is that the gradient of solar radiation is smaller at the south, where the solar incidence angles get close to 0. According to (2), the radiation difference is minor for small incidence angles. Therefore, the slight difference of temperature measurement will significantly affect slope estimation.

5. Experiments

The proposed method was also validated in a controlled outdoor environment on August 30 and December 11, 2017. Figure 11 shows the experimental setup. Silica sand layers were formed on slanted surfaces of 0, 10 and 20 [deg] on August 30 and 0, 5, 15 and 25 [deg] on December 11. The thermal insulating sheet was placed under the layers to avoid heat transmission to the ground. The location is the same as the previous simulation. The direction of slopes is 180 [deg] (south-facing slope). The solar incidence angles under these conditions can be computed as shown in Table 2.

The sand layers were continuously exposed to the sunlight from 0:00 pm to 3:00 pm. The surface temperatures were measured every minute with an infrared camera and a thermometer. The DNI is estimated at each time by applying the following model from [10] to the flat plane measurement

$$S_{w\downarrow} = l/(4.57 \times 54) \tag{10}$$

where l denotes illuminance measured by an illuminometer.

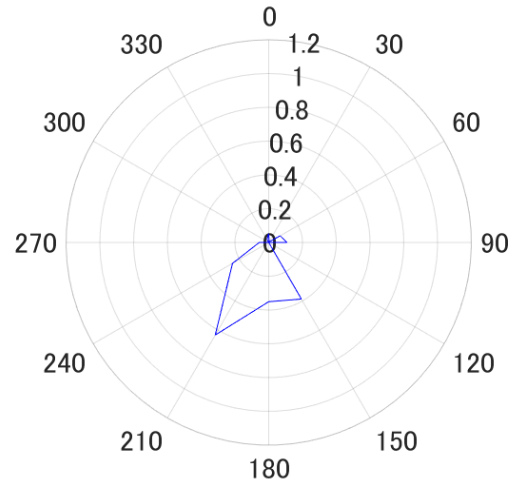

(a) 9:00 am

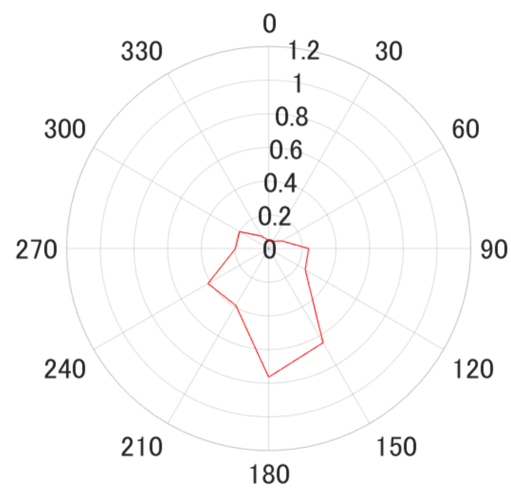

(b) 0:00 pm

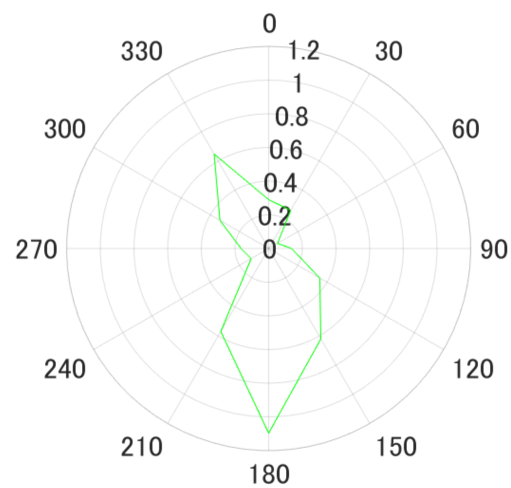

(c) 3:00 pm

Figure 10. Direction sensitivity in estimation accuracy [deg]

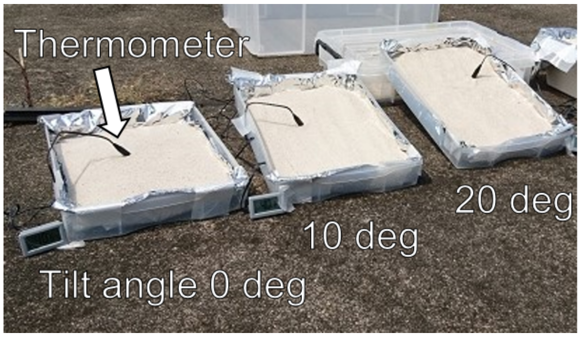

Figure 11. Experimental setup taken on August 30

Table 3. Experimental parameters. JMA represents the dataset from Japan Meteorological Agency.

Name	Symbol	Value
Surface albedo	A	0.20
Surface emissivity	ϵ	0.90
Heat capacity	C_p	1.00 $[\mathrm{kJ/(kg \cdot K)}]$
Air density	ρ	1.21 $[\mathrm{kg/m^3}]$
Heat exchange coefficient	$C_H U$	0.015 $[\mathrm{m/s}]$
Air temperature	T_a	JMA
Atmospheric radiation	$L_{w\downarrow}$	JMA

Model verification

As a preliminary experiment, actual temperature measurements and model-based estimations were compared in order to verify the validity of the energy balance equation and the experimental assumption. Table 3 summarizes the model parameters used for the verification. A comparison of model and measured temperatures is shown in Figure 12. It is seen that the temperature estimation from the energy model fits the measurements from the external sensor. The root mean square error of temperature was 1.83 [°C]. This error is similar to that of [8], therefore this result indicates that the adopted model and assumptions are appropriate for this experimental setup.

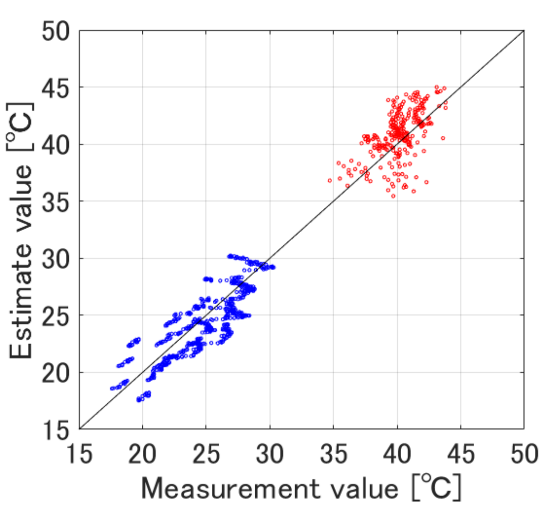

Figure 12. Comparison between measured and estimated surface temperatures (red:August 30, blue:December 11)

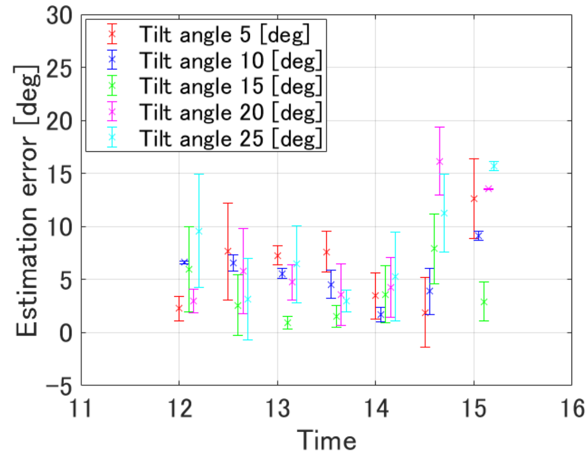

Figure 13. Absolute angle error in outdoor experiment (error bar is SD of absolute error). Tilt angle 10 and 20 [deg] are on August 30, Tilt angle 5, 15 and 25 [deg] are on December 11.

Slope estimation results

Slope angles were estimated based on temperature measurements from a target slope (5, 10, 15, 20, 25 [deg]) and a reference plane (0 [deg]). The slope estimation results are shown in Figure 13. Most of the errors are around 2–7 [deg] until a sudden drop in accuracy to >10 [deg] around 14:30 pm. This performance degradation can be explained by the change in weather conditions: increased clouds at the time reduced the radiation that reaches the ground.

Discussions

The proposed method could successfully estimate slope angles solely from temperature measurements. The obtained accuracy is sufficient to detect untraversable steep slopes. However, there might be applications that requires higher accuracy such as kinematics-based traversablity analysis. Below are discussions regarding accuracy improvement.

Weather dependency The ground surface temperature could be unexpectedly affected by changes in weather conditions. Cloudiness is an example seen in the experiment. The surface temperature change introduces the inconsistency with the precomputed solar radiation data, thereby increasing the error in slope angle estimation. The impact of weather changes can be mitigated by monitoring sudden changes in ground temperature. Also, it should be noted that this effect is minor in planets such as Mars where the weather conditions rarely change.

Model improvement A simplified energy model is used in the algorithm for the sake of computational efficiency. As a side effect, a few energy terms are neglected which may reduce the model fidelity. A detailed examination of thermal models could improve the accuracy.

Parameters identification There is uncertainty in parameter identification which significantly affects the slope estimation. An accurate parameter identification method is important to achieve high accuracy. An interesting approach would be a machine learning-based parameter identification, which updates the parameters based on the existing measurements.

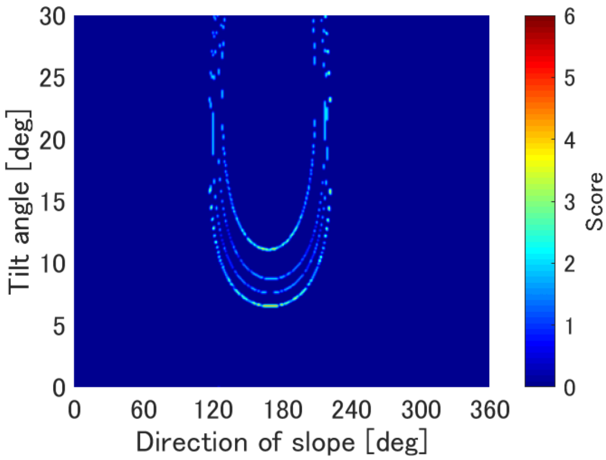

Figure 14. An example of failure in estimation due to the fact that the contours have no intersection point

Measurement noise There are some cases where the slope angle cannot be estimated since the contours have no intersection point, as illustrated in Figure 14. Among the possible causes, the measurement noise in temperature is considered significant. This failure can also happen because of the unexpected change of surface temperature due to weather conditions. One approach to handle this noise is to adopt a robust scoring method in the surface normal selection process. In practice, it is straightforward to detect this types of failure and invoke recovery actions.

6. SUMMARY

This paper has presented a slope estimation method using a monocular infrared camera with an application to planetary exploration rovers. A differential energy model is developed to correlate the geometry of distant terrain to thermal properties in target and reference terrains. A set of possible slope parameters is obtained from remote temperature measurements using our differential model. A scoring-based method from continuous observations enables the reliable estimation of slope parameters at any solar and slope direction.

The proposed method was validated by simulations and outdoor experiments. In the simulation, the average error was nominally less than 1 [deg] during the daytime. In the outdoor experiments, most of the errors were around 2-7 [deg] in nominal conditions, its accuracy being sensitive to global environmental changes. Despite unavoidable ambiguity in measurements and parameter identification, the proposed method accurately recovers the slope angles.

The approach described in this paper can be improved from several aspects. Firstly, high-fidelity energy model could be used. This requires the accurate identification terrain and aerial parameters. The high-fidelity model would be useful for the assessment of more complex terrain. Secondly, the surface geometry selection process can be made more robust to noise by using robust scoring techniques. Further investigation on the selection process may relax the constraints on the number of required measurements, allowing a slope estimation with fewer data points.

REFERENCES

[1] S. B. Goldberg, M. W. Maimone, and L. Matthies, "Stereo vision and rover navigation software for planetary exploration," *IEEE Aerospace Conference*, vol. 5, pp. 2025–2036, 2002.

[2] K. Schauwecker, R. Klette, and A. Zell, "A new feature detector and stereo matching method for accurate high-performance sparse stereo matching," *IEEE/RSJ International Conference on Intelligent Robots and Systems*, pp. 5171–5176, 2012.

[3] Z. F. Wang and Z. G. Zheng, "A region-based stereo matching algorithm using cooperative optimization," *IEEE Conference on Computer Vision and Pattern Recognition*, pp. 1–8, 2008.

[4] H. Hirschmuller and D. Scharstein, "Evaluation of Stereo Matching Costs on Images with Radiometric Differences," *IEEE Transactions on Pattern Analysis and Machine Intelligence*, vol. 31, no. 9, pp. 1582–1599, 2009.

[5] G. Ishigami, M. Otsuki, and T. Kubota, "Path planning and navigation framework for a planetary exploration rover using a laser range finder," *Field and Service Robotics*, vol. 92, pp. 431–447, 2014.

[6] R. Zhang, P. S. Tsai, J. E. Cryer, and M. Shah, "Shape-from-Shading: a survey," *IEEE Transactions on Pattern Analysis and Machine Intelligence*, vol. 21, no. 8, pp. 690–706, 1999.

[7] M. K. Johnson and E. H. Adelson, "Shape estimation in natural illumination," *IEEE Conference on Computer Vision and Pattern Recognition*, pp. 2553–2560, 2011.

[8] Martin J. Best, "A model to predict surface temperatures," *Boundary-Layer Meteorology*, vol. 88, no. 2, pp. 279–306, 1998.

[9] The Japan Meteorological Agency Web site: `http://www.jma.go.jp/jma/indexe.html` [Accessed at 16_{th} October 2017].

[10] R. W. Thimijan and R. D. Heins, "Photometric, radiometric, and quantum light units of measure: a review of procedures for interconversion," *HortScience*, vol. 18, no. 6, pp. 818–822, 1983.

BIOGRAPHY

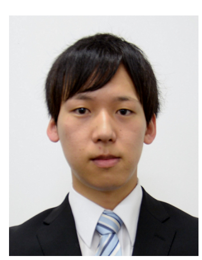

Satoshi Watanabe *received the B.S. degree from the Department of Precision Mechanics, Chuo University, Tokyo, Japan, in 2016. He is currently pursuing the master's degree with the Graduate School of Science and Engineering, Chuo University. His main research interest is environment recognition for planetary exploration rovers. He is a member of the Japan Society of Mechanical Engineers.*

Kyohei Otsu received his Bachelor's, Master's., and Ph.D. degrees in Electrical Engineering from the University of Tokyo in 2011, 2013, and 2016, respectively. In 2016, he joined Jet Propulsion Laboratory as a Robotics Technologist in the Mobility and Robotic Systems Section. His technical expertise includes visual perception, localization, motion planning, and autonomous learning.

Masatsugu Otsuki *was born in Japan in 1977. He received his Bachelor's, Master's, and Doctorate degrees from Keio University in 2000, 2001, and 2005, respectively. From 2002 to 2005, he worked as an Assistant Professor at the Department of System Design Engineering, Keio University. He is currently working as an Assistant Professor at the Department of Spacecraft Engineering in Institute of Space and Astronautical Science, Japan Aerospace Exploration Agency. He is a member of the JSME and RSJ. His current research interests include mobility and dynamics of a spacecraft and a planetary rover.*

Takashi Kubota *is a professor at Institute of Space and Astronautical Science (ISAS), Japan Aerospace Exploration Agency (JAXA), Japan. He received Dr. degree in electrical engineering in 1991 from the University of Tokyo. He is also a professor of the graduate school of the University of Tokyo. He was a visiting scientist in Jet Propulsion Laboratory in 1997 and 1998. He engaged in the guidance, navigation, and control in HAYABUSA mission. His research interests include Robotics and AI in space, especially Autonomous Rover and Image based Navigation etc.*

Gakuto Masuyama *received a B.S. degree in Engineering from Nagoya University, Japan, in 2005; he also earned M.S. and Ph.D. degrees in Engineering from the University of Tokyo, Japan, in 2007 and 2013, respectively. Since 2013, he has been an Assistant Professor at Chuo University, then moved to Meijo University as an Associate Professor in 2017. His research interests include perceptual information processing and intelligent robotics. He is a member of the IEEE and RSJ.*

Kazunori Umeda *received B.Eng., M.Eng., and Ph.D. degrees in precision machinery engineering from the University of Tokyo, Japan, in 1989, 1991 and 1994 respectively. He became a Lecturer of Precision Mechanics at Chuo University, Japan in 1994, and is currently a Professor since 2006. He was a visiting worker at National Research Council of Canada from 2003 to 2004. His research interests include robot vision, 3D vision, and human interface using vision.*